nature physics

Article

https://doi.org/10.1038/s41567-025-02838-4

Circadian coupling orchestrates cell growth

Received: 31 May 2024

Accepted: 20 February 2025

Published online: 31 March 2025

Check for updates

Nica Gutu[1,2], Malthe S. Nordentoft[3], Marlena Kuhn[1], Carolin Ector[1,2], Marie Möser[1], Anna-Marie Finger[1], Mathias Spliid Heltberg[3], Mogens Høgh Jensen[3], Ulrich Keilholz[1,4], Achim Kramer[1], Hanspeter Herzel[2,5] & Adrián E. Granada[1,4]

Single-cell circadian oscillators exchange extracellular information to sustain coherent circadian rhythms at the tissue level. The circadian clock and the cell cycle couple within cells but the mechanisms underlying this interplay are poorly understood. We show that the loss of extracellular circadian synchronization disrupts circadian and cell cycle coordination within individual cells, impeding collective tissue growth. We use the theory of coupled oscillators combined with live population, and single-cell recordings and precise experimental perturbations. Coherent circadian rhythms yield oscillatory growth patterns, which unveil a global timing regulator of tissue dynamics. Knocking out core circadian elements abolishes the observed effects, highlighting the central role of circadian clock regulation. Our results underscore the role of tissue-level circadian disruption in regulating proliferation, thereby linking disrupted circadian clocks with oncogenic processes. These findings illuminate the intricate interplay between circadian rhythms, cellular signalling and tissue physiology and enhance our understanding of tissue homeostasis and growth regulation in the context of both health and disease.

Due to Earth's rotation, organisms experience cyclical environmental changes associated with day and night cycles. In response, most organisms have evolved an internal circadian clock to anticipate and coordinate physiological and metabolic processes with the environmental cycles[1,2]. In humans, the circadian clock operates through a hierarchical organization, wherein a master clock in the hypothalamic suprachiasmatic nucleus coordinates the activities of peripheral autonomous clocks distributed across the body[3]. At the single-cell level, the molecular clock machinery relies on autoregulatory transcription–translation feedback loops that consist of both positive and negative elements. This feedback drives the cyclic expression of clock genes and proteins with a period of around 24 h (refs. 4,5).

Peripheral clocks show rhythmicity independently of the suprachiasmatic nucleus[6–8]. The synchronization of individual circadian oscillators within peripheral tissues ensures that individual cellular clocks are synchronized, which allows tissues to maintain coherent tissue-wide rhythms characterized by distinct oscillatory strengths[9,10]. The mechanisms underlying this peripheral tissue coupling are an active field of research, with evidence indicating that several mechanisms could contribute to it in a tissue-specific manner. Coupling through hormonal pathways, such as glucocorticoid signalling[11] and paracrine signalling with molecules like transforming growth factor β (TGFβ), have been shown to play a role in this process[12,13]. Feeding cycles can entrain peripheral clocks independently of the suprachiasmatic nucleus, indicating the presence of food-responsive oscillators[14]. Additionally, molecular feedback loops through intracellular signalling ensure rhythmic synchronization, which prevents disruption to tissue-level circadian function. This combination of local, hormonal and systemic cues ensures robust circadian coupling in peripheral tissues (Fig. 1a).

In proliferating cells, there is another main regulatory biological process, the cell cycle, which has a comparable characteristic period of 24 h. This process involves a series of ordered and regulated

[1]Charité Universitätsmedizin Berlin, Berlin, Germany. [2]Humboldt Universität zu Berlin, Berlin, Germany. [3]Niels Bohr Institute, University of Copenhagen, Copenhagen, Denmark. [4]German Cancer Consortium (DKTK), Berlin, Germany. [5]Institute for Theoretical Biology, Berlin, Germany.
e-mail: adrian.granada@charite.de

https://doi.org/10.1038/s41567-025-02838-4

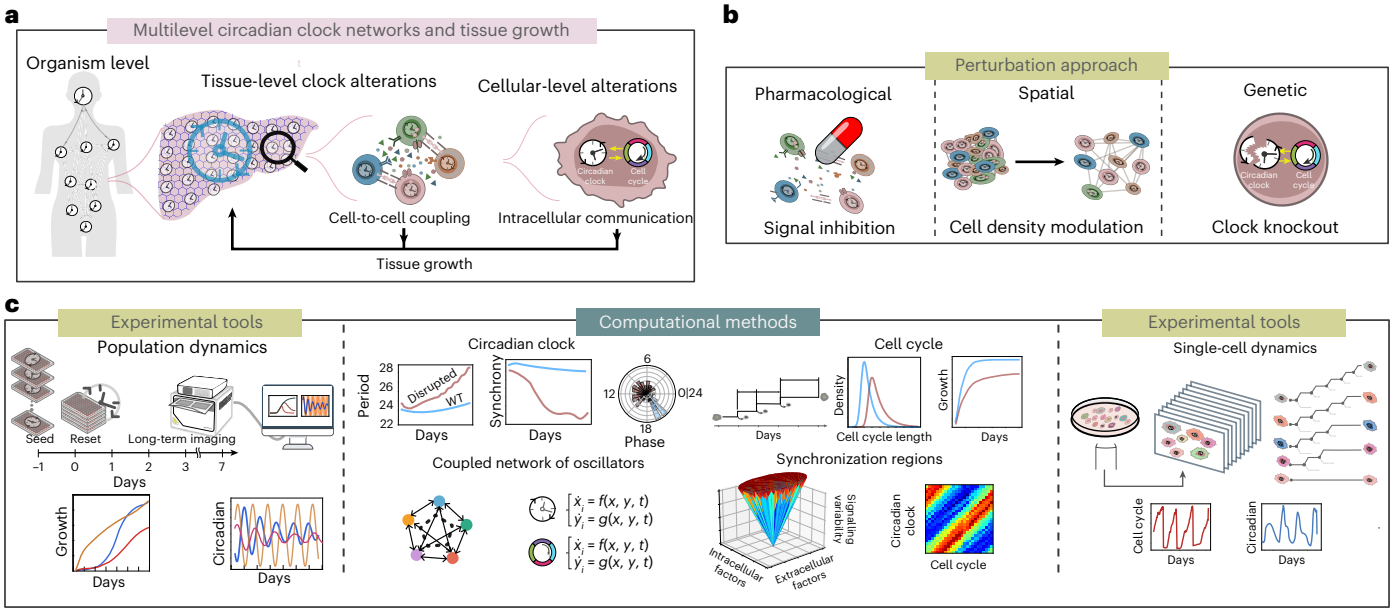

Fig. 1 | Framework for identifying extracellular and intracellular circadian and cell cycle interactions. a, Schematic of human circadian clock networks. The master clock coordinates peripheral clocks across the body. Peripheral clocks form a network at the tissue level and exchange signals. At the single-cell level, the circadian clock and cell cycle are robustly coupled. Tissue-level and within-cell communications are expected to affect collective tissue. **b**, Our perturbation approach for disrupting cellular communications includes the pharmacological inhibition of circadian signals, spatial cell density modulation and the genetic knockdown of circadian clock components. **c**, Combined experimental and computational tools for studying population and single-cell dynamics. We used long-term live imaging at both levels analysed with diverse time-series tools and integrated this approach with coupled oscillator theory and computational single-cell models. WT, wild type.

events involving cell growth, DNA replication and division and with distinct phases such as G1 (gap 1), S (DNA synthesis), G2 (gap 2) and M (mitosis)[15–18]. The stepwise progression through recurring phases of activation and repression and successive divisions can be conceptualized as another periodic process[19].

Hence, at the single-cell level, two periodical biological processes with analogous periods coexist and interact[20–26]. These resemble two oscillators that are capable of coupling and synchronization, with important physiological implications for tissue homeostasis and cancer (reviewed in ref. 27). Pioneering in vivo studies indicate that there is circadian regulation of cell proliferation in tissues such as blood, bone marrow, gastrointestinal mucosa, skin and liver. The rhythms are influenced by glucocorticoid levels and regeneration processes[28–32]. However, there are numerous questions, including on the nature and directionality of the coupling between the circadian clock and the cell cycle and, most importantly, how extracellular factors regulate this intracellular coupling across tissues.

This study investigates the synchronization role of the extracellular circadian clock in the intracellular communication between the cell cycle and the circadian clock. To address this question, we employed various strategies to disrupt extracellular circadian coupling, namely pharmacological perturbations, cell density control to diminish the amount of circadian information exchanged in the media and genetic disruption of the circadian clock (Fig. 1b). Moreover, we built a mathematical model and performed long-term live-imaging recordings at the single-cell and population levels of the human osteosarcoma cell line (U2OS), a well-established in vitro model of human peripheral clocks (Fig. 1c).

Results

Circadian coupling enhances locking with the cell cycle

To comprehend how the heterogeneity within an ensemble of circadian clocks influences their synchronization, we simulated a network of Poincaré oscillators[33,34]. In this ensemble, each circadian clock has an individual period and influences all the others (mean field)[35]. We constructed a diagram to determine the regions of entrainment by measuring the network synchronization index while varying the dispersions of the period distribution and the coupling strengths (Fig. 2a,b). On decreasing the extracellular couplings, marked as 4 to 1 in the plot, we observed gradually dampened oscillations (Fig. 2b,c and Supplementary Fig. 1a,b) with a period prolongation proportional to the extracellular coupling values (Table 1). The abbreviations Table 1 are defined as follows: t_f represents the simulation time, dt is the numerical integration step size, N denotes the number of simulated oscillators, and extra and intra refer to the extracellular and intracellular coupling values, respectively. To quantify the damping of the oscillations, we calculated the phase coherence, which decays proportionally to the coupling strength due to an increase in the dispersion of phases over time (Fig. 2c). The synchronization index and phase coherence provide complementary insights: the synchronization index reflects the time-averaged collective behaviour, whereas the phase coherence captures dynamic changes in phase alignment.

To test these predictions, we disrupted the extracellular circadian coupling with an inhibitor of the TGFβ pathway (LY2109761) or by reducing the seeding density. The circadian and cell cycle signals of the cells were consistently monitored over 5 days. Subsequently, an automated pipeline developed for ilastik (ref. 36) was employed to track thousands of cells. Following the exclusion of noisy, non-oscillating cells, around 3,000 cells remained, from which approximately 90% were oscillating with similar periods over the different conditions (Supplementary Fig. 1c–e and Methods). The untreated cells exhibited damped oscillations, attributed to population de-phasing, consistent with the characteristics expected from the U2OS cell line model of peripheral clocks (Fig. 2d). The inhibitor of the TGFβ pathway (LY2109761) diminished the population circadian amplitude and accelerated this damping. The period was prolonged in a dose-dependent manner (Fig. 2d). However, at the single-cell level, this drug did not reduce the amplitude (Supplementary Figs. 1f,g and 2a–d). Upon comparison with simulations (Fig. 2a–c), we observed a parallelism between the addition of the inhibitor and the reduction of extracellular circadian

coupling strength. Notably, we observed differences in the circadian period prolongation between this study and our previous work[37], which potentially arose from variations in the detection measurement and parametrization methods. Our current study has focused on single-cell fluorescence data from individual cells, whereas our previous study used whole-population bioluminescence recordings.

An alternative method for attenuating the coupling strength within a network of circadian clocks interacting through a mean field is to decrease the seeding density. Thus, we first extracted the single-cell traces and confirmed that the circadian rhythm oscillated robustly in time (Supplementary Fig. 2a,e,f). Voronoi diagrams were employed to assess the network structure and quantify the cell density (Supplementary Fig. 3a and Methods). This analysis indicated that smaller Voronoi cell areas are correlated with higher seeding densities, indicating that the seeding density can be employed to modulate the spatial distribution of cells (Supplementary Fig. 3b,c). This approach yielded analogous density-dependent outcomes (Fig. 2e and Supplementary Fig. 3d).

Next, to explore the interplay between the extracellular circadian coupling and the intracellular circadian cell cycle locking, we expanded our simulated network by coupling a cell cycle oscillator to each circadian oscillator (Fig. 2f). To assess the level of intracellular locking between the circadian clock and the cell cycle, we calculated the phase differences between these two rhythms for each simulated cell unit. To quantify the synchronization of the intracellular locking, we measured the phase coherence of these phase differences. After the initial transient stage, during which the oscillators evolved from the initial conditions to their corresponding final state, the phase coherence stabilized around a mean value depending on the interplay between the extracellular and the intracellular couplings (Supplementary Fig. 4a and Methods). A high mean phase coherence of the phase difference between the circadian clock and the cell cycle indicates internal locking and overall synchronization. By increasing the extracellular coupling, we obtained a higher global synchronization of the circadian clock and the cell cycle communication (Fig. 2g top left). In parallel, we measured the fraction of cells with a locked intracellular circadian clock and cell cycle. These cells had a stable phase difference during the second half of the simulation, for both uncoupled and well-coupled circadian clocks (Fig. 2g right and Supplementary Fig. 4b). Furthermore, we constructed a phase-space representation for uncoupled and well-coupled circadian clocks (Fig. 2h). In an ensemble of uncoupled circadian clocks, the phases of the two rhythms were dispersed across the entire phase space to form trajectories with different phase differences (Fig. 2h bottom). Increasing the extracellular coupling led to the emergence of attractors, which indicate the conservation of a specific phase difference across the network that is modulated by the communication among circadian clocks (Fig. 2h top). Altogether, our findings reveal that increasing the extracellular circadian coupling enhanced the synchronization of intracellular circadian and cell cycle communication.

During the single-cell experiments perturbing the extracellular circadian coupling through the LY2109761 inhibitor or the seeding density, we collected instantaneous circadian and cell cycle rhythms (Fig. 2i). The untreated cells exhibited an initial peak in the circadian phase coherence after the phase resetting, which was followed by desynchronization, consistent with our simulations and the observations outlined in ref. 37 (Fig. 2j). The treated cells reached the peak faster and started desynchronization earlier, thus achieving the minimum phase coherence sooner (Fig. 2j). Hence, pharmacological inhibition of the TGFβ pathway accelerated the loss of circadian synchronization.

To evaluate the extent of intracellular communication between the circadian clock and the cell cycle for untreated cells, we depicted the two-dimensional distribution of their phases, which revealed robust patterns of phase-locking (Fig. 2k top left). This observation implies that well-coupled circadian oscillators maintain strong phase-locking with the cell cycle. However, when the communication among the circadian clocks was perturbed with the TGFβ pathway inhibitor drug or by manipulating the seeding density, the circadian phases no longer exhibited a discernible preference for the timing of division events, thus destroying the phase-locking patterns (Fig. 2k top right and Supplementary Fig. 3c). We simulated more realistic interactions by incorporating parameter heterogeneity and bidirectionality in the model (Supplementary Fig. 4d,e and Methods). Our analysis of phase-locking patterns yielded comparable results, indicating that a relatively simple asymmetric model can provide important insights into the interplay between extracellular synchronization and the intracellular coupling of the circadian clock and cell cycle.

To measure the difference in phase-locking patterns, we calculated the correlation coefficient between the two-dimensional distributions (Methods). This analysis revealed a dose-dependent reduction like that in the untreated scenario in response to TGFβ pathway inhibitor with similar outcomes for the reduction of the seeding density (Supplementary Fig. 4f).

Moreover, the temporal dynamics of circadian desynchronization resemble the decoherence of phase differences between the circadian and cell cycle and the detuning of their periods (Supplementary Fig. 4g). By splitting the experiment into two stages—one characterized by high circadian phase coherence and the other by low phase coherence—we altered the overall phase-locking patterns between the circadian rhythm and the cell cycle (Fig. 2k bottom). Collectively, these results indicate the possibility of manipulating the global phase-locking dynamics between the circadian rhythm and the cell cycle by modulating the extracellular circadian coupling. This manipulation could be achieved with a TGFβ pathway inhibitor drug, by adjusting the seeding density or by time decoherence.

Fig. 2 | Extracellular circadian coupling modulates the intracellular relation with the cell cycle. a, Sketch of mean-field coupled circadian oscillators with period distribution. **b**, Left, colour-coded fraction of synchronized oscillators versus period dispersion and extracellular coupling strength. Right, population amplitude for increasing coupling strength (points 1–4). **c**, Population period (top) and phase coherence (bottom) for coupling strengths from **b**. **d**, Left, population circadian amplitude of U2OS-RevErbα cells over 5 days with coupling inhibitor LY2109761 (colour-coded). Right, corresponding period evolution. Sample sizes, $n = 923$ (0 μM), $n = 1{,}856$ (5 μM) and $n = 759$ (10 μM). **e**, Left, experimental circadian amplitude for different seeding densities. Right, circadian period for different seeding densities. Sample sizes, $n = 923$ (yellow), 294 (green) and 89 (blue). **f**, Sketch of extracellular circadian coupling, intracellular circadian and cell cycle coupling, and phase diagram with two locking states. **g**, Three-dimensional diagrams of entrainment regions for coupled circadian oscillators. Top, simulated synchronization heat map for intracellular (z axis) and extracellular (y axis) coupling strengths. Colour-coding shows the locking index (purple to pink; Methods). Bottom, three-dimensional depiction of **b** (left) showing circadian dispersion (x axis) versus extracellular coupling (y axis) at zero intracellular coupling ($z = 0$). Right, simulated intracellular entrainment regions for high (extra = 0.7) and low (extra = 0) extracellular coupling. Colour-coding represents the fraction of locked circadian and cell cycle oscillators. **h**, Simulated phase-locking heat maps of circadian and cell cycle rhythms for well-coupled oscillators (high extracellular coupling, extra = 0.7) and poorly coupled oscillators (low extracellular coupling, extra = 0). Colour-coding indicates phase density. **i**, Top, snapshots of the circadian signal of a cell initially, post-mitosis and finally. Bottom, corresponding circadian signal with division times (dashed lines). **j**, Circadian phase coherence for different inhibitor concentrations. The dashed line splits the experiment into two halves (sample sizes as in **d**). **k**, Top, phase-locking heat maps of circadian and cell cycle rhythms for two conditions (same sample sizes as **d**). Bottom, untreated cells in the first (left) and second half (right) of the experiment, corresponding to states of high and low phase coherence (**j** and Supplementary Fig. 4g). conc., concentration; EC, extracellular coupling; osc, oscillators; $TGF\beta_i$, TGFβ inhibitor.

https://doi.org/10.1038/s41567-025-02838-4

Extracellular circadian synchronization modulates cell growth

To delve deeper into the impact of extracellular circadian coupling on the cell cycle, we modulated the extracellular circadian coupling with an inhibitor of the TGFβ pathway (LY2109761), by decreasing the seeding density or by genetically disrupting the circadian clock and monitored population growth (Fig. 3a). We measured growth in terms of population confluence while manipulating the extracellular coupling with the LY2109761 drug. The results show dose-dependent saturation levels and doubling times (Fig. 3b left, Supplementary Fig. 5a and Supplementary Tables 1 and 2). Recent studies indicate that the TGFβ

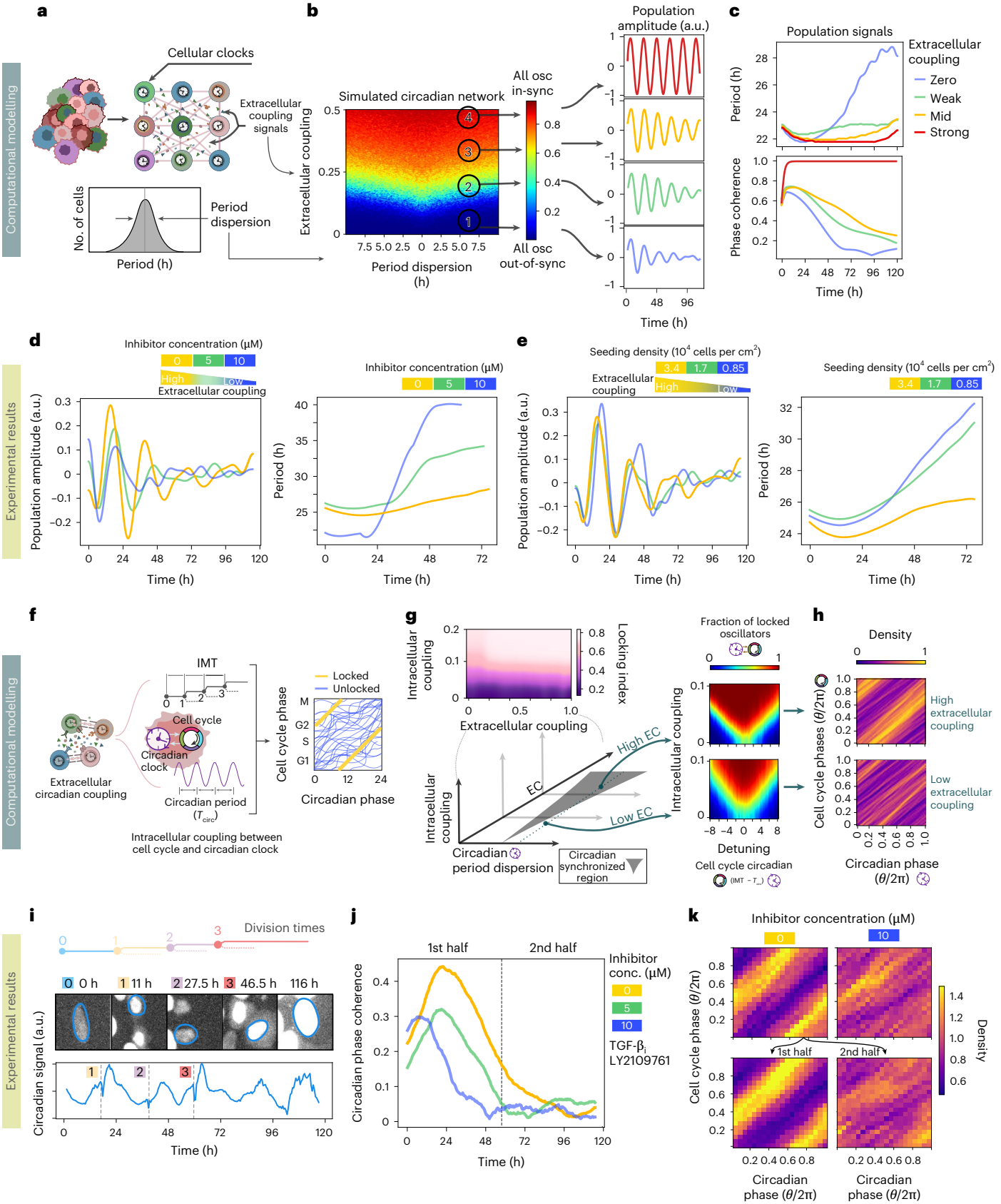

https://doi.org/10.1038/s41567-025-02838-4

Table 1 | Simulation parameters of the Poincaré model

Figure	t_f	dt	N	Extra	$Intra_{circ→cc}$
Fig. 2b	120 h	0.1 h	200	0–0.5	-
Figs. 2b,c and 4f–h and Supplementary Figs. 1a,b and 6e,g	120 h	0.1 h	200	0 (blue), 0.05 (green), 0.075 (yellow) and 0.5 (red)	-
Fig. 2g (top)	300 h	0.1 h	200	0–1.0	0–0.2
Fig. 2g (right)	200 h	0.1 h	200	0 (uncoupled) and 0.7 (coupled)	0–0.1
Fig. 2h and Supplementary Fig. 4b	500 h	0.1 h	200	0 (uncoupled), and 0.7 (coupled)	0.01
Supplementary Fig. 4a	120 h	0.1 h	200	0.7 (light pink and light purple) and 0 (dark pink and dark purple)	0.15 (light pink and dark pink) and 0 (light purple and dark purple)

inhibitor LY2109761 may affect cell motility, which could delay the attainment of full confluency[38–40]. Thus, the observed dose-dependent saturation levels may be caused by a drug-induced reduction in cell motility. Notably, cells with well-coupled circadian clocks proliferated faster compared to cells with disrupted extracellular circadian communication (Fig. 3c). At the population level, the circadian signal of untreated cells revealed a more robust coupling among cells, which manifested a long-term sustained oscillation, unlike cells treated with the extracellular inhibitor (Supplementary Fig. 5b).

These results could be attributed to a circadian modulation of cellular growth or other potential effects of the TGFβ pathway inhibitor drug. To distinguish between these scenarios, we computed the growth as measured by the confluency while modulating the extracellular circadian coupling with the seeding density. We hypothesized that reducing the quantity of extracellular circadian signals in the media and, hence, the extracellular circadian coupling would lead to reduced growth. Cells with the lowest seeding density also had longer doubling times (Fig. 3b (right) and Fig. 3c). High-seeded cells exhibited a robust and prolonged circadian oscillation compared to the low-seeded cells, which also had higher damping and lengthening of the circadian period (Supplementary Fig. 5c).

We used two distinct approaches—drug dose modulation and cell density modulation—as proxies to disrupt cell-to-cell communication and investigate the potential effects of circadian synchronization on cell proliferation. Although these methods differ fundamentally, we used them as complementary tools to explore how circadian desynchronization could influence growth. Notably, we observed that the growth differences resulting from modulating the drug dose versus altering the seeding density did not correspond in a one-to-one manner (Fig. 3b,c), underscoring their distinct effects on cellular behaviour. To gain a deeper understanding of these different impacts on proliferation, we tracked division events in hundreds of individual cells, following the method detailed in ref. 41, and we recorded the timing of each division event (Methods). Our analysis revealed considerable heterogeneity in cell proliferation, with subpopulations dividing between 1 and 5 times. Interestingly, we observed that the distribution of these proliferative subgroups exhibited similar trends under both reduced cell density and increased drug concentrations, our two proxies for modulating cell-to-cell communication (Supplementary Fig. 5d). Furthermore, when examining the intermitotic time (IMT) across these subgroups, we consistently found that the length of the cell cycle tended to increase with both higher inhibitor doses and lower seeding densities, highlighting a parallel effect in prolonging the duratioin of the cell cycle across both modulations (Supplementary Fig. 5e).

To understand whether the observed growth differences might potentially be ascribed to circadian modulation, we tested the effects of LY2109761 in two U2OS cell lines: a wild-type cell line with a properly functioning circadian clock (used in the aforementioned experiments) and a variant cell line with a dysfunctional clock, namely Cry1/2 double knockout[42] (Fig. 3a right and Supplementary Fig. 5f)[43]. We compared the growth of untreated cells from both cell lines for 5 days and found that they had similar proliferation rates (Fig. 3d, Supplementary Fig. 5g,h and Supplementary Tables 3 and 4). Then, we compared the impact of the drug on both cell lines by computing the relative growth between the treated and untreated cells in each case. This uncovered a higher impact in the cells with a properly functioning circadian clock (Fig. 3e). This experiment showed that the U2OS wild-type cells with the TGFβ pathway inhibitor proliferated less compared to untreated cells, whereas the double-knockout cells exhibited similar proliferation rates irrespective of the presence of the drug (Fig. 3e and Supplementary Table 5). These results illustrate that the inhibitor affected cell proliferation only in the presence of a functional circadian clock. When the clock was dysfunctional, as in the U2OS Cry1/2 double-knockout cell line, the inhibitor did not modify the growth dynamics because the communication pathways that could be disrupted by the TGFβ inhibitor were no longer operative, leading to similar division rates in the presence or absence of the drug. Hence, these data indicate that the inhibitor was not the dominant factor driving the observed changes in proliferation through potential cytotoxic or growth-related effects, but that these effects rely on an active circadian clock.

To broaden the scope of our findings beyond tumour cell lines, we conducted further experiments using NIH3T3 mouse embryonic fibroblasts, HEK293T human embryonic kidney cells and HaCaT human keratinocytes. These experiments successfully replicated our key observations regarding extracellular circadian coupling and its impact on cell growth. Specifically, modulating the extracellular circadian communication by inhibiting the TGFβ pathway revealed noticeable differences in growth patterns between treated and control cells (Supplementary Fig. 5j). As expected, considering that the time for these cell lines to double in number was higher than the circadian period[25,44–57], their growth rate was reduced due to the disrupted communication in the presence of the drug. These findings indicate that our conclusions may be generalizable to non-tumour cell lines, indicating that circadian coupling regulates cell growth. Nevertheless, further investigations are required to comprehensively elucidate the generalization of the circadian clock control over proliferation.

Growth curves show 24-h oscillations

To discern the source of the growth differences and to avoid effects due to the averaging of population measures, we examined the single-cell proliferation while disrupting extracellular circadian coupling using the TGFβ pathway inhibitor LY2109761. The cells displayed a heterogeneous proliferation pattern, spanning from no proliferation to high proliferation (Fig. 4a). To understand the impact of the inhibitor on the cell cycle, we computed the IMTs of the tracked cells throughout the entire recording. The distribution of the IMTs shifted to higher values as the concentration of the inhibitor increased (Fig. 4b).

To study the evolution of proliferation over time, we quantified the cumulative distribution of division events. We observed a higher proliferation rate in the untreated cells compared to the treated cells (Fig. 4c and Supplementary Table 6). To prevent overemphasizing specific lineages, which might obscure the differences between conditions, we also counted the cells over time, which revealed even more pronounced dose-dependent growth changes (Supplementary Fig. 6a and Supplementary Table 7). These growth differences can be explained by longer IMTs and fewer divisions in the population subjected to high concentrations of LY2109761, as their circadian clocks were weakly coupled. Strikingly, oscillations of approximately 24 h were evident in the growth of the cell population with well-coupled circadian clocks,

https://doi.org/10.1038/s41567-025-02838-4

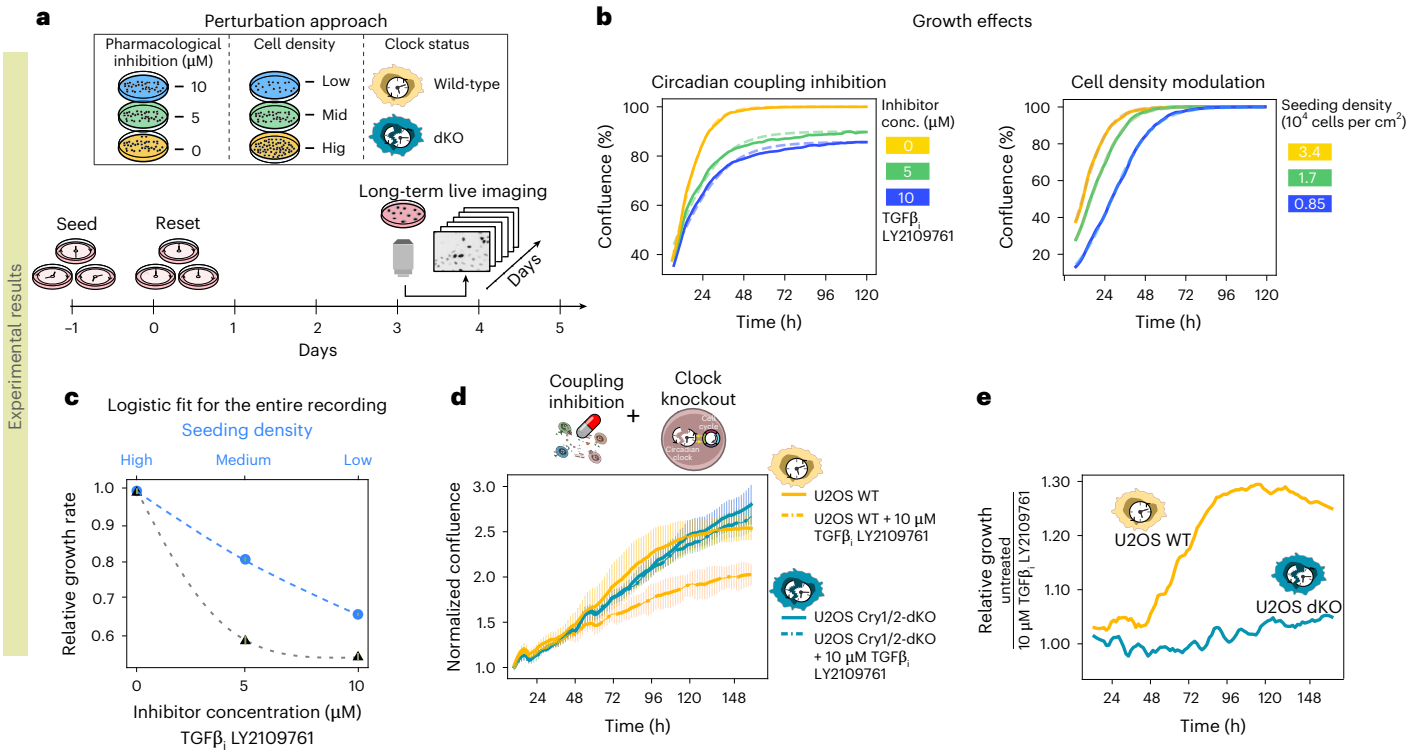

Fig. 3 | Extracellular circadian coupling controls the growth rate. a, Long-term live-imaging set-up used to record the growth while inhibiting the extracellular circadian coupling. We used the inhibitor LY2109761, the seeding density and genetic disruption of the circadian clock. **b**, Confluency recorded for 5 days under different concentrations of the extracellular circadian coupling inhibitor (left) and different initial seeding densities (right). The curves were fitted (dashed lines) to a sigmoidal growth function to extract the growth rates (Methods and Supplementary Table 1). **c**, Relative growth rates (mean value) obtained from fitting the growth curves in **b** and using the propagation error formula (for exact values; see Supplementary Table 1). Error bars (standard errors) are shown on the markers. The dashed lines are the growth rates fitted to an exponential function. **d**, Normalized confluence (mean value) with error bars (standard deviation) derived from three technical replicates monitored for 168 h for two U2OS cell lines: wild type (yellow) and double knockout of *Cry1/2* (turquoise). Untreated cells are represented as a continuous line. Cells treated with the coupling inhibitor are shown as dashed lines. The corresponding growth rates from the fitting to the sigmoidal growth function are shown in Supplementary Table 3. **e**, Relative growth of wild-type cells (yellow) and the double-knockout cells (turquoise) measured by the confluence ratio between untreated and 10 μM LY2109761 treated conditions. The growth rates from the fitting of the sigmoidal growth function are shown in Supplementary Table 5.

indicating that the cells proliferated synchronously with a periodicity of 24 h (Fig. 4c,d). To distinguish more clearly the 24-h oscillations in growth, we detrended the curve of the cumulative distribution of cell divisions. This approach revealed a more rapid damping of oscillations when circadian coupling was reduced by the inhibitor drug, leading to an extended period (Fig. 4d). Different seeding densities showed analogous outcomes (Supplementary Fig. 6b–d and Supplementary Table 8).

Next, to gain a complementary understanding of how extracellular circadian communication affects growth, we extended our mathematical model by incorporating a stochastic cell cycle model (Methods). To study different interactions between the circadian clock and the cell cycle, we tested for two qualitatively different scenarios (Fig. 4e): (1) with a circadian clock that modulates the rate of cell cycle progression and subsequently the length of the cell cycle (scenario 1) and (2) with a circadian clock that modulates the transition between cell cycle phases, which can be seen as a gating mechanism (scenario 2). To model these two scenarios, we examined the modulation of the G1 phase in scenario 1 and the S phase transition in scenario 2. However, the results described here are general and broadly illustrate a phase-speed versus phase-transition scenario, regardless of the specific cell cycle phase being modulated. Modulating the phase speed through a coupling in the G1 phase gave results that are consistent with our single-cell experiments (Fig. 4b–d and Supplementary Fig. 6e). The intermitotic period distributions and growth rate were affected by a decrease in the extracellular circadian coupling strength (Figs. 4f,g and Supplementary Fig. 6f,g). Conversely, when the coupling was added to the S transition, no substantial impact on growth or IMTs was observed (Fig. 4f,g and Supplementary Fig. 6f). Thus, our model indicates a scenario in which the circadian clock modulates the rate of a cell cycle phase.

Finally, to incorporate more realistic interactions, parameter heterogeneity was introduced into the model. Our simulations showed that the cumulative growth patterns remained robust across different parameter distributions (Supplementary Fig. 6g). Minor variations in growth curves were observed, but these were primarily attributed to stochastic fluctuations in the model, reinforcing our belief that the observed growth dynamics are not sensitive to specific parameter choices (see Methods for simulation details).

Discussion

To synchronize with cyclic environmental conditions, organisms have evolved a molecular endogenous timing system of 24 h, the circadian clock, which couples extracellularly to maintain coherence. Simultaneously, cellular division takes place to support growth and preserve homeostasis. Within numerous cells, these two internal rhythms operate concurrently with mechanisms of interactions yet to be uncovered. In this work, we address the impact of circadian synchronization on cell growth.

To understand the effect of extracellular circadian synchronization on the intracellular communication between the circadian clock and the cell cycle, we built a mathematical model using Poincaré oscillators. Our observations revealed that a well-coupled functional network of circadian clocks heightened the communication between

https://doi.org/10.1038/s41567-025-02838-4

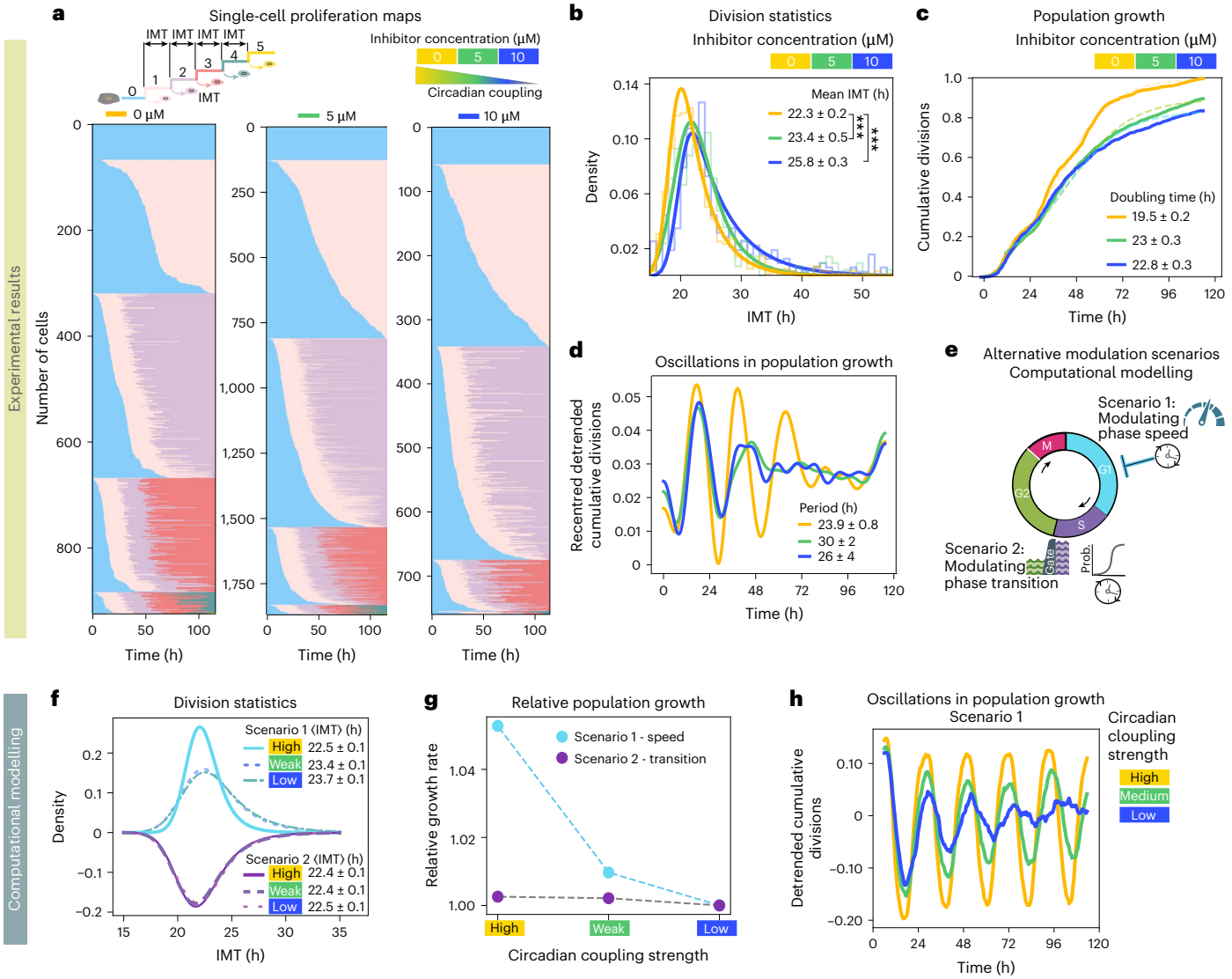

Fig. 4 | Synchronization of circadian clock modulates the length of the cell cycle. a, Single-cell proliferation maps for the extracellular coupling inhibitor LY2109761. Each row shows the division activity of an individual cell, with each mitotic event marked by a colour transition (colour-coding top left). Cells are clustered by the number of divisions and then sorted by their first mitosis time. **b**, IMT distribution of the cells tracked from the beginning of the recording for different inhibitor concentrations. The legend shows the mean and error from the fitting to an exponential modified Gaussian. A Kolmogorov–Smirnov two-sided test was performed to compare each treated distribution to the untreated population, without several comparison adjustments. The stars indicate the following *P* values: 2.5×10^{-12} (green-yellow) and 4×10^{-14} (blue-yellow). Sample sizes, 0 μM ($n = 654$), 5 μM ($n = 910$) and 10 μM ($n = 343$). **c**, Cumulative distribution of divisions for different inhibitor concentrations with bootstrapping ($n = 750$). The curves were fitted to a sigmoidal growth function (dashed lines). The legend shows the doubling times corresponding to the growth rates (Supplementary Table 6). **d**, Recentred detrended cumulative distribution of the division events from **c** for different inhibitor concentrations. The periods of the observed oscillations are shown in the legend. **e**, Mathematical model for growth dynamics contemplating two possible scenarios for the circadian modulation of cell cycle: modulating the phase speed (scenario 1) and modulating the cell cycle phase transition (scenario 2). **f**, Histogram of fitted IMTs for different simulated circadian coupling strengths. Scenario 1 is for the circadian rhythm coupled to the G1 phase (blue). Scenario 2 is for the circadian coupled at the S transition (violet and on a flipped second axis). The legend shows the means and errors from the fitting to an exponential modified Gaussian. For a model description and parameters, see Methods. **g**, Relative growth rates of simulated cell cycles for different extracellular circadian coupling strengths when the circadian rhythm was coupled to the G1 phase (blue) or the S transition (violet). The change is the ratio between the growth rate of a particular coupling strength and its value at zero strength. **h**, Detrended simulated cumulative distribution of divisions for different circadian coupling strengths.

the cell cycle and the circadian clock. Furthermore, we found that a population phase-locked between the circadian clock and the cell cycle can be disrupted through extracellular circadian communication using a TGFβ secretory pathway inhibitor or by changing the seeding density. Together, these findings highlight the potential role of the circadian clock on cell cycle regulation by showing that stronger coupling between circadian clocks leads to more robust phase-locking.

Further experiments indicated that by altering the extracellular circadian coupling with the TGFβ secretory pathway inhibitor, we could modify the growth rate of the population. To discard the attribution of growth differences to the toxic or proliferative effects of the inhibitor, we explored the effect of changes to the seeding density as an alternative and observed analogous results. To gain a deeper understanding of the observed variations in growth, we investigated growth in two U2OS cell lines: a wild-type cell line and a cell line with a disrupted circadian clock (U2OS Cry1/2-dKO BMAL1-Luc). The former cell line had a double knockout of two core clock genes, *Cry1* and *Cry2* (refs. 42). The addition of the TGFβ secretory pathway inhibitor changed the growth rate

in the wild-type cell line. However, the drug produced no substantial changes in the double-knockout cell line. Hence, a population of cells with functional and synchronized circadian clocks exhibited enhanced proliferation compared to a cell line with a disrupted circadian clock. Taken together, these findings highlight the importance of extracellular circadian communication and synchronization in orchestrating growth. The length of the cell cycle adapts to the circadian rhythm and neither accelerates nor decelerates due to the 1:1 phase-locking between the circadian clock and the cell cycle, forcing proliferation rates to mirror the circadian periods.

On the population level, these growth differences could mask different cell cycle outcomes ranging from cell cycle arrest to death. To discern the proliferation behaviour from other possibilities, we explored division events at the single-cell level under the influence of the LY2109761 drug or by manipulating the seeding density. In both instances of disrupting the extracellular circadian synchronization, we observed diminished proliferation rates compared to the well-coupled circadian clock scenario. Moreover, the division events showed discernible oscillations, indicating that cells divided synchronously and periodically every approximately 24 h. These oscillations exhibited modified periods and quicker damping when the extracellular circadian coupling was disturbed.

By expanding the Poincaré model to include a stochastic cell cycle component, we gained insights into how circadian rhythms and population synchrony are interconnected. Specifically, we found that the length of the cell cycle, modulated by the coupled circadian rhythm, plays a key role in driving differences in growth rates for the model. When the circadian period became out of synchronization, so did the progression of the cell cycle, leading to a loss of synchrony in cell division across the population.

In summary, our study elucidates the interplay between the circadian clock and the cell cycle, and specifically, how the circadian clock can modulate cellular growth. Our findings indicate that cell growth can be affected by disturbing the extracellular circadian coupling. After knocking out fundamental circadian components, there were negligible growth changes upon disruption of the extracellular circadian synchronization. Altogether, these results reveal the timing mechanism of the circadian clock as an orchestrator of the dynamics of tissue growth. The circadian clock determines a time window for the length of the cell cycle due to the 1:1 locking between the circadian and cell cycle rhythms.

In other words, disrupting the circadian intercellular coupling drove cells to exit a locked state. In this desynchronized state, cell cycle oscillators reverted to their intrinsic free-running periods, which can influence proliferation positively or negatively depending on the cellular context and baseline IMT distribution. For U2OS cells, this shift resulted in slower growth due to their longer intrinsic IMTs, whereas for cells with an intrinsic IMT distribution shorter than 24 h, our simulations predicted that shorter free-running IMTs would accelerate growth (Supplementary Fig. 7). These simulations indicate that disrupting the circadian coupling could modulate the growth dynamics through synchronization-dependent mechanisms.

It is important to note that disrupting the circadian clock can impact growth through different mechanisms. For example, Huber et al.[58] demonstrated that disrupting intrinsic clock components, like Cry2, enhances proliferation through intracellular pathways, specifically through c-MYC degradation. This contrasts with our study, as we found that growth is affected by disrupted intercellular synchronization, emphasizing distinct levels of circadian regulation with unique impacts on proliferation.

We strategically used U2OS cells due to their well-characterized intrinsic oscillatory properties and recent advances in understanding extracellular coupling[37]. Because of the availability of pharmacological tools that modulate coupling states combined with the suitability of these cells for long-term single-cell live imaging, we could conduct precise temporal behaviour analyses, which enhanced the technical rigour and reproducibility of our experiments. We recapitulated a few of our key results using non-tumour cells. Using three non-tumour cell line models, we successfully replicated our key findings to demonstrate how disrupting circadian communication impacts cell growth. This was achieved by modulating intercellular coupling with a TGFβ receptor inhibitor. However, we acknowledge the limitation of relying on a few cell line models, and future studies should explore other cell types to broaden the experimental context and validate our findings across diverse systems.

By elucidating how multiscale coordination among circadian clocks regulates cellular proliferation at the population level, this study represents a remarkable conceptual advance. Our findings reveal that intercellular coupling between circadian clocks plays a critical role in maintaining synchronization across the population and the locking with the cell cycle within individual cells. When this coupling is disrupted, individual circadian clocks desynchronize, leading to a breakdown of the cell cycle–circadian locking states at the population level. As shown experimentally and through simulations, the loss of this synchronization allows individual cell cycle oscillators to revert to their intrinsic 'free-running' periods, as reflected in the variability of IMTs. Thus, the degree of synchronization among circadian clocks modulates the length of the cell cycle. This extracellular coupling can be used to tune proliferation, indicating that an organism can alter its growth dynamics by adjusting the communication between its circadian clocks. In pathological contexts, such as disease, any disruption of this synchrony leads to an uncoupled and desynchronized ensemble, in which individual cells revert to autonomous, free-running intermitotic periods, thus highlighting the critical role of circadian coherence in maintaining time-coordinated cell division.

These initial findings lay the groundwork for unravelling the molecular mechanisms. Further experiments are required to characterize the regulatory pathways involved. Potential contributors to this orchestration include Wee1, MYC, p16 and p21 (refs. 27,59). Inhibitors targeting these molecular mechanisms could be employed to evaluate their impact on the interplay between the circadian clock and the cell cycle. The growth and homeostasis of biological systems rely on the meticulous regulation of the cell cycle. Disruption leads to uncontrolled proliferation and, eventually, tumorigenesis. The potential ability to decelerate fast divisions within tumours to 24-h cell cycle lengths by manipulating the extracellular circadian clock communication holds an important promise for various cancer therapies.

Online content

Any methods, additional references, Nature Portfolio reporting summaries, source data, extended data, supplementary information, acknowledgements, peer review information; details of author contributions and competing interests; and statements of data and code availability are available at https://doi.org/10.1038/s41567-025-02838-4.

References

1. Chaix, A., Zarrinpar, A. & Panda, S. The circadian coordination of cell biology. *J. Cell Biol.* **215**, 15–25 (2016).
2. Dunlap, J. C. Molecular bases for circadian clocks. *Cell* **96**, 271–290 (1999).
3. Mohawk, J. A., Green, C. B. & Takahashi, J. S. Central and peripheral circadian clocks in mammals. *Annu. Rev. Neurosci.* **35**, 445–462 (2012).
4. Takahashi, J. S. in *A Time for Metabolism and Hormones* (eds Sassone-Corsi, P. and Christen, Y.) 13–24 (Springer, 2016).
5. Pett, J. P., Kondoff, M., Bordyugov, G., Kramer, A. & Herzel, H. Co-existing feedback loops generate tissue-specific circadian rhythms. *Life Sci. Alliance* https://doi.org/10.26508/lsa.201800078 (2018).
6. Tahara, Y. et al. In vivo monitoring of peripheral circadian clocks in the mouse. *Curr. Biol.* **22**, 1029–1034 (2012).

7. Saini, C. et al. Real-time recording of circadian liver gene expression in freely moving mice reveals the phase-setting behavior of hepatocyte clocks. *Genes Dev.* **27**, 1526–1536 (2013).
8. Sinturel, F. et al. Circadian hepatocyte clocks keep synchrony in the absence of a master pacemaker in the suprachiasmatic nucleus or other extrahepatic clocks. *Genes Dev.* **35**, 329–334 (2021).
9. Yoo, S. H. et al. PERIOD2::LUCIFERASE real-time reporting of circadian dynamics reveals persistent circadian oscillations in mouse peripheral tissues. *Proc. Natl Acad. Sci. USA* **101**, 5339–5346 (2004).
10. Abraham, U. et al. Coupling governs entrainment range of circadian clocks. *Mol. Syst. Biol.* **6**, 438 (2010).
11. Le Minh, N., Damiola, F., Tronche, F., Schütz, G. & Schibler, U. Glucocorticoid hormones inhibit food-induced phase-shifting of peripheral circadian oscillators. *EMBO J.* **20**, 7128–7136 (2001).
12. Finger, A.-M. & Kramer, A. Peripheral clocks tick independently of their master. *Genes Dev.* **35**, 304–306 (2021).
13. Buhr, E. D. & Takahashi, J. S. in *Circadian Clocks* (eds Kramer A. & Merrow, M.) 3–27 (Springer, 2013).
14. Damiola, F. et al. Restricted feeding uncouples circadian oscillators in peripheral tissues from the central pacemaker in the suprachiasmatic nucleus. *Genes Dev.* **14**, 2950–2961 (2000).
15. Feillet, C., van der Horst, G. T. J., Levi, F., Rand, D. A. & Delaunay, F. Coupling between the circadian clock and cell cycle oscillators: implication for healthy cells and malignant growth. *Front. Neurol.* **6**, 96 (2015).
16. Schafer, K. A. The cell cycle: a review. *Vet. Pathol.* **35**, 461–478 (1998).
17. Golias, C. H., Charalabopoulos, A. & Charalabopoulos, K. Cell proliferation and cell cycle control: a mini review. *Int. J. Clin. Pract.* **58**, 1134–1141 (2004).
18. Satyanarayana, A. & Kaldis, P. Mammalian cell-cycle regulation: several Cdks, numerous cyclins and diverse compensatory mechanisms. *Oncogene* **28**, 2925–2939 (2009).
19. Hunt, T. & Sassone-Corsi, P. Riding tandem: circadian clocks and the cell cycle. *Cell* **129**, 461–464 (2007).
20. Gérard, C. & Goldbeter, A. Entrainment of the mammalian cell cycle by the circadian clock: modeling two coupled cellular rhythms. *PLoS Comput. Biol.* **8**, e1002516 (2012).
21. Droin, C., Paquet, E. R. & Naef, F. Low-dimensional dynamics of two coupled biological oscillators. *Nat. Phys.* **15**, 1086–1094 (2019).
22. Glass, L. & Mackey, M. C. *From Clocks to Chaos* (Princeton Univ. Press, 1988).
23. Yang, Q., Pando, B. F., Dong, G., Golden, S. S. & van Oudenaarden, A. Circadian gating of the cell cycle revealed in single cyanobacterial cells. *Science* **327**, 1522–1526 (2010).
24. Feillet, C. et al. Phase locking and multiple oscillating attractors for the coupled mammalian clock and cell cycle. *Proc. Natl Acad. Sci. USA* **111**, 9828–9833 (2014).
25. Bieler, J. et al. Robust synchronization of coupled circadian and cell cycle oscillators in single mammalian cells. *Mol. Syst. Biol.* **10**, 739 (2014).
26. Bratsun, D. A., Merkuriev, D. V., Zakharov, A. P. & Pismen, L. M. Multiscale modeling of tumor growth induced by circadian rhythm disruption in epithelial tissue. *J. Biol. Phys.* **42**, 107–132 (2016).
27. Gaucher, J., Montellier, E. & Sassone-Corsi, P. Molecular cogs: interplay between circadian clock and cell cycle. *Trends Cell Biol.* **28**, 368–379 (2018).
28. Smaaland, R., Sothern, R. B., Laerum, O. D. & Abrahamsen, J. F. Rhythms in human bone marrow and blood cells. *Chronobiol. Int.* **19**, 101–127 (2002).
29. Bjarnason, G. A. & Jordan, R. Circadian variation of cell proliferation and cell cycle protein expression in man: clinical implications. *Prog. Cell Cycle Res.* **4**, 193–206 (2000).
30. Bjarnason, G. A. et al. Circadian expression of clock genes in human oral mucosa and skin: association with specific cell-cycle phases. *Am. J. Pathol.* **158**, 1793–1801 (2001).
31. Brown, W. R. A review and mathematical analysis of circadian rhythms in cell proliferation in mouse, rat, and human epidermis. *J. Investig. Dermatol.* **97**, 273–280 (1991).
32. Barbason, H. et al. Circadian synchronization of liver regeneration in adult rats: the role played by adrenal hormones. *Cell Prolif.* **22**, 451–460 (1989).
33. Winfree, A. T. Biological rhythms and the behavior of populations of coupled oscillators. *J. Theor. Biol.* **16**, 15–42 (1967).
34. Winfree, A. T. *The Geometry of Biological Time* (Springer, 1980).
35. Kuramoto, Y. *Chemical Oscillations, Waves, and Turbulence* Vol. 19 (Springer, 1984).
36. Berg, S. et al. ilastik: interactive machine learning for (bio)image analysis. *Nat. Methods* **16**, 1226–1232 (2019).
37. Finger, A.-M. et al. Intercellular coupling between peripheral circadian oscillators by TGF-β signaling. *Sci. Adv.* **7**, eabg5174 (2021).
38. Yang, M. et al. TGF-β-Induced FLRT3 attenuation is essential for cancer-associated fibroblast-mediated epithelial-mesenchymal transition in colorectal cancer. *Mol. Cancer Res.* **20**, 1247–1259 (2022).
39. Melisi, D. et al. LY2109761, a novel transforming growth factor beta receptor type I and type II dual inhibitor, as a therapeutic approach to suppressing pancreatic cancer metastasis. *Mol. Cancer Ther.* **7**, 829–840 (2008).
40. Kim, S., Lee, J., Jeon, M., Lee, J. E. & Nam, S. J. Zerumbone suppresses the motility and tumorigenecity of triple negative breast cancer cells via the inhibition of TGF-β1 signaling pathway. *Oncotarget* **7**, 1544–1558 (2016).
41. Gutu, N., Binish, N., Keilholz, U., Herzel, H. & Granada, A. E. p53 and p21 dynamics encode single-cell DNA damage levels, fine-tuning proliferation and shaping population heterogeneity. *Commun. Biol.* **6**, 1196 (2023).
42. Börding, T., Abdo, A. N., Maier, B., Gabriel, C. & Kramer, A. Generation of human CrY1 and Cry2 knockout cells using duplex CRISPR/Cas9 technology. *Front. Physiol.* **10**, 449711 (2019).
43. Ector, C. et al. Time-of-day effects of cancer drugs revealed by high-throughput deep phenotyping. *Nat. Commun.* **15**, 7205 (2024).
44. Rahimi, A. M. et al. Expression of α-tubulin acetyltransferase 1 and tubulin acetylation as selective forces in cell competition. *Cells* **10**, 390 (2021).
45. Nagoshi, E. et al. Circadian gene expression in individual fibroblasts: cell-autonomous and self-sustained oscillators pass time to daughter cells. *Cell* **119**, 693–705 (2004).
46. Kaeffer, B. & Pardini, L. Clock genes of mammalian cells: practical implications in tissue culture. *In Vitro Cell. Dev. Biol.: Anim.* **41**, 311–320 (2005).
47. Li, N. et al. Suprachiasmatic nucleus slices induce molecular oscillations in fibroblasts. *Biochem. Biophys. Res. Commun.* **377**, 1179–1184 (2008).
48. Rogers, P. M., Ying, L. & Burris, T. P. Relationship between circadian oscillations of *Rev-erbα* expression and intracellular levels of its ligand, heme. *Biochem. Biophys. Res. Commun.* **368**, 955–958 (2008).
49. Abaandou, L., Quan, D. & Shiloach, J. Affecting HEK293 cell growth and production performance by modifying the expression of specific genes. *Cells* **10**, 1667 (2021).
50. Erzurumlu, Y., Catakli, D. & Dogan, H. K. Circadian oscillation pattern of endoplasmic reticulum quality control (ERQC) components in human embryonic kidney HEK293 cells. *J. Circadian Rhythms* **21**, 1 (2023).

51. Shende, V. R., Goldrick, M. M., Ramani, S. & Earnest, D. J. Expression and rhythmic modulation of circulating microRNAs targeting the clock gene *Bmal1* in mice. *PLoS ONE* **6**, e22586 (2011).
52. Zheng, L., Seon, Y. J., McHugh, J., Papagerakis, S. & Papagerakis, P. Clock genes show circadian rhythms in salivary glands. *J. Dent. Res.* **91**, 783–788 (2012).
53. Beta, R. A. A. et al. Core clock regulators in dexamethasone-treated HEK 293T cells at 4 h intervals. *BMC Res. Notes* **15**, 23 (2022).
54. Ramanathan, C., Khan, S. K., Kathale, N. D., Xu, H. & Liu, A. C. Monitoring cell-autonomous circadian clock rhythms of gene expression using luciferase bioluminescence reporters. *J. Vis. Exp.* https://doi.org/10.3791/4234 (2012).
55. Pessina, A. et al. High sensitivity of human epidermal keratinocytes (HaCaT) to topoisomerase inhibitors. *Cell Prolif.* **34**, 243–252 (2001).
56. Spörl, F. et al. A circadian clock in HaCaT keratinocytes. *J. Investig. Dermatol.* **131**, 338–348 (2011).
57. Matsunaga, N. et al. 24-hour rhythm of aquaporin-3 function in the epidermis is regulated by molecular clocks. *J. Investig. Dermatol.* **134**, 1636–1644 (2014).
58. Huber, A.-L. et al. CRY2 and FBXL3 cooperatively degrade c-MYC. *Mol. Cell* **64**, 774–789 (2016).
59. Qu, M. et al. Circadian regulator BMAL1::CLOCK promotes cell proliferation in hepatocellular carcinoma by controlling apoptosis and cell cycle. *Proc. Natl Acad. Sci. USA* **120**, e2214829120 (2023).

Methods

Materials and experimental set-up

Fluorescent reporter cell lines. U2OS cells express a fusion protein NR1D1::VNP, which comprises a nuclear localization signal and PEST element fused to the open reading frame of Venus, with the addition of the 116 N-terminal amino acids of NR1D1, as detailed in ref. 45. Cells were generously provided by M. Brunner from Heidelberg University. A single subclone derived from this cell line was selected for subsequent experimental investigations. Stable expression of a cell cycle reporter CFP-hGeminin was obtained by lentiviral transduction followed by clonal selection. For all experiments, freshly thawed and early passage clonal cells were used, specifically between passage numbers P3 and P6.

Cell culture. U2OS cells were grown in RPMI medium containing l-glutamine (R8758, Sigma), supplemented with 10% fetal bovine serum (FBS, Capricorn Scientific 12A) and 1% antibiotic–antimycotic solution (Gibco15240096). For the NIH3T3, HEK293T and HaCaT cells, Dulbecco's modified Eagle's medium (DMEM)/F12 (1:1) supplemented with 10% FBS was used as the stock solution. The DMEM/F12 already contained 15 mM HEPES and L-glutamine. For the cell lines NIH3T3 and HaCaT, the stock solution was supplemented with 1% HEPES (to reach a final concentration of 25 mM HEPES), and 1% penicillin-streptomycin was added. For the HEK293T cells, that stock solution was supplemented with 1% penicillin-streptomycin only.

Generation of reporter cell lines. Details of the generation of the U-2 OS-Cry1/Cry2-dKO cell line can be found in the original publication[42]. U2OS wild-type and Cry1/Cry2-dKO were provided by A. K.'s laboratory. HaCaT keratinocytes were gifted from Dr Fusenig's laboratory at Deutsches Krebsforschungsinstitut, Heidelberg, Germany. NIH3T3 cells were purchased from the American Type Culture Collection. HEK293T cells were gifted by the Lahav Lab, Harvard Medical School.

Resetting. Resetting was achieved through incubation with 1 µM dexamethasone (dissolved in ethanol; Sigma-Aldrich) for 30 min under standard tissue culture conditions. After the incubation period, the dexamethasone was completely removed. The cells were thoroughly washed with phosphate-buffered saline in preparation for subsequent downstream applications. We specifically used a short pulse of dexamethasone to avoid the cytotoxic and cytostatic effects seen in ref. 60.

Receptor inhibitor. TGFβ receptor inhibitor LY2109761 was prepared following the manufacturer's guidelines. It was dissolved in the recommended solvents and stored at −20 °C. The drug was administered at the specified concentrations during the seeding, after the resetting and during imaging. The inhibitor persisted in the medium from its introduction throughout the entire duration of the experiment. The inhibitor LY2109761 and its solvent control (dimethyl sulfoxide) were introduced into a conditioned medium. The inhibitor was purchased from Cayman Chemical (15409).

Microscopy. U2OS NR1D1::VNP reporter cells were cultured in FluoroBrite medium, which was composed of FluoroBrite DMEM (high glucose, without HEPES; Thermo Fisher Scientific A1896701) and supplemented with 2% FBS, 1% penicillin-streptomycin and l-glutamine (300 mg l^{-1}; Thermo Fisher Scientific, 25030149) for long-term live imaging.

Single-cell live imaging was achieved with high-resolution multichannel fluorescence microscopy using a high-resolution multichannel wide-field epi-fluorescence Nikon Ti2 microscope equipped with an environmental chamber for cell cultures (Okolab) and using the software NIS-Elements visualization (Nikon). Images were acquired at 30-min intervals over several days using a ×20 Plan Apo Ph2 DM λ magnification objective (Nikon), light-emitting diode illumination (Lumencor, SPECTRA X) and a camera with a scientific complementary–metal–oxide semiconductor active-pixel sensor (PCO). Live imaging of a population was conducted with a prolonged, low-resolution incubator-embedded microscope (Incucyte, Essen Bioscience). In each experiment, there were biological and technical replicates.

Luciferase reporter assays. To assess circadian rhythms, we employed U2OS cells stably expressing a Bmal1-luciferase reporter, which was kindly provided by A.K.'s laboratory. This cell line was developed to facilitate real-time monitoring of circadian gene expression through luminescence measurements, as detailed in their publication[42].

Image analysis

ilastik. First, for each image sequence, we preprocessed the images to increase the brightness and contrast with the histogram equalization function in the Python skimage package, specifically the exposure function. To enhance the continuous visualization of the cell nuclei, we overlapped the images from the circadian and cell cycle channels (Supplementary Fig. 8). To perform single-cell tracking, we used a modular software framework, ilastik (v.1.4.0b21-OSX)[36], which comprises several blocks: an initial training phase involving automated (supervised) pixel- and object-level classification, automated and semi-automated object tracking, semi-automated segmentation, and object counting. We chose a representative image sequence to construct training files for segmentation and tracking in ilastik, following the approach outlined in ref. 61. The pixel classification workflow distinguished cells from the background. The segmentation output was employed for tracking with the learning workflow, using optimized parameters tailored to our image dataset and an adaptative threshold for signal detection. For signal quantification, we used raw image sequences from the circadian and cell cycle channels individually and extracted the intensity values using ilastik as well. Finally, the object classification workflow was applied to extract the mean signal intensities. The subsequent batch processing was then run.

Incucyte. For each frame, an image analysis was conducted to count nuclei using the embedded software Incucyte (2022A, Essen BioScience) within the Live-Cell Analysis Systems. This process facilitated the acquisition of confluency data as well as the quantification of reporter signal counts. The imaging pipeline was carefully designed and iteratively refined to define masks that accurately captured the cell confluence. These masks were optimized and tested across various time points, cell density concentrations, plate positions and experimental conditions. This rigorous iterative approach minimized inaccuracies stemming from crowding effects to ensure that our confluence measurements reliably reflected the cell growth dynamics.

Computational methods

Filtering the signals. Traces containing more than 100 frames (equivalent to 50 h) were selectively retained for subsequent analyses. Discrepancies in the size of the nucleus between consecutive frames were quantified to identify instances of erroneous tracking and merging cells. Traces exhibiting a change in nucleus size surpassing 500 pixels were excluded, except in cases associated with cell division. Within each lineage, pairwise comparisons of circadian signal read-outs were executed, leading to the removal of traces with a similarity exceeding 80%, as these were attributed to late division events. Cells with at least one peak were kept for the subsequent data analysis. Only traces with a continuous wavelet transform power exceeding 5% of the median power distribution were retained for subsequent analyses.

Division events. If the peaks in the gradient of the cell cycle signal exhibited abrupt changes and surpassed three times the mean of the gradient, they were defined as cell division events. These are discernible alterations in the Gemini fluorescent signal.

Preprocessing single-cell signals. Individual circadian signals were extracted from the single-cell experiment and detrended with the function sinc_detrend (with a cutoff period of 50 h) and the amplitude was normalized with the function normalize_amplitude (with a window size of 50 h) from the pyBOAT package of Python[62]. This uses a sinc filter that removes periods larger than a certain cutoff. The cell cycle signals were not preprocessed. Finally, the cells were ranked based on their circadian power, and only those exceeding a threshold of 10 were included in the subsequent analysis.

Continuous wavelet transforms. We computed the continuous wavelet transforms using the functions compute_spectrum, get_maxRidge and ridge_data from the open-source software package pyBOAT. By detecting ridges in individual signals, we identified the predominant oscillatory elements in the range 16 to 40 h, which were characterized by having the highest power.

Poincaré model

To simulate the circadian clock and cell cycle signals, we employed Poincaré equations for the circadian clock with a mean-field coupling (extra) and an intracellular coupling for the cell cycle and the circadian clock (intra):

$$\begin{cases} \frac{\mathrm{d}(\mathrm{circ}_i)}{\mathrm{d}t} = -\lambda(\mathrm{circ}_i)(A_\mathrm{o} - \mathrm{circ}_i) + \frac{\mathrm{extra}}{N}\sum_{j=1}^{N}\mathrm{circ}_j + \mathrm{intra}_{\mathrm{cc}\to\mathrm{circ}}(\mathrm{circ}_i), \\ \frac{\mathrm{d}\phi_i}{\mathrm{d}t} = \frac{2\pi}{T_{\mathrm{circ}_i}}, \end{cases} \quad (1)$$

$$\begin{cases} \frac{\mathrm{d}(\mathrm{cc}_i)}{\mathrm{d}t} = -\gamma(\mathrm{cc}_i)(B_\mathrm{o} - \mathrm{cc}_i) + \mathrm{intra}_{\mathrm{circ}\to\mathrm{cc}}(\mathrm{circ}_i), \\ \frac{\mathrm{d}\theta_i}{\mathrm{d}t} = \frac{2\pi}{\mathrm{IMT}_i}, \end{cases} \quad (2)$$

In equation 1: i represents an oscillator; circ_i represents the radial component of a circadian oscillator; λ is the relaxation parameter for a circadian oscillator; A_o is the radius of the limit cycle for a circadian oscillator; N is the total number of oscillators; φ_i represents the angular velocity component of a circadian oscillator; T_{circ_i} stands for the circadian ocillator period. In equation 2: cc_i stands for the radial component of the cell cycle oscillator; γ represents the relaxation paramenter for a cell cycle oscillator; B_o is the radius of the limit cycle for a cell cycle oscillator; θ_i is the angular velocity component of a cell cycle oscillator. These equations were transformed to Cartesian coordinates using $r = \sqrt{x^2 + y^2}$ and $\varphi = \mathrm{atan}\, y/x$:

$$\begin{cases} \frac{\mathrm{d}(X_i)}{\mathrm{d}t} = -\lambda\left(\sqrt{X_i^2 + Y_i^2} - A_\mathrm{o}\right)X_i - \frac{2\pi}{T_{\mathrm{circ}_i}}Y_\mathrm{i} + \frac{\mathrm{extra}}{2N}\sum_{j=1}^{N}X_j + \mathrm{intra}_{\mathrm{cc}\to\mathrm{circ}}(XX_i), \\ \frac{\mathrm{d}(Y_i)}{\mathrm{d}t} = -\lambda\left(\sqrt{X_i^2 + Y_i^2} - A_\mathrm{o}\right)Y_i + \frac{2\pi}{T_i}X_\mathrm{i} + \frac{\mathrm{extra}}{2N}\sum_{j=1}^{N}Y_j + \mathrm{intra}_{\mathrm{cc}\to\mathrm{circ}}(YY_i), \end{cases} \quad (3)$$

$$\begin{cases} \frac{\mathrm{d}(XX_i)}{\mathrm{d}t} = -\gamma\left(\sqrt{XX_i^2 + YY_i^2} - B_\mathrm{o}\right)XX_i - \frac{2\pi}{\mathrm{IMT}_i}YY_i + \mathrm{intra}_{\mathrm{circ}\to\mathrm{cc}}(X_i), \\ \frac{\mathrm{d}(YY_i)}{\mathrm{d}t} = -\gamma\left(\sqrt{XX_i^2 + YY_i^2} - B_\mathrm{o}\right)XX_i + \frac{2\pi}{\mathrm{IMT}_i}XX_i + \mathrm{intra}_{\mathrm{circ}\to\mathrm{cc}}(Y_i), \end{cases} \quad (4)$$

where X_i and Y_i are the Cartesian coordinates corresponding to the circadian clock and XX_i and YY_i to the cell cycle. The model incorporates bidirectional intracellular coupling between the circadian clock and the cell cycle. For simplicity, an asymmetry was introduced in the model, and some figures (Figs. 2b,c,g,h and 4f–h, Supplementary Figs. 4a,b,d,e and 6e–g) were generated under the condition $\mathrm{intra}_{\mathrm{cc}\to\mathrm{circ}} = 0$. To account for the bidirectionality in Supplementary Fig. 4e, we considered int $\mathrm{ra}_{\mathrm{cc}\to\mathrm{circ}} = \mathrm{intra}_{\mathrm{circ}\to\mathrm{cc}} = 0.1$. To study the influence of each term of the bidirectionality in Supplementary Fig. 4c, we considered two scenarios: one with $\mathrm{intra}_{\mathrm{cc}\to\mathrm{circ}} = 0$ and $\mathrm{intra}_{\mathrm{circ}\to\mathrm{cc}} = 0.1$ (middle plot) and another with the $\mathrm{intra}_{\mathrm{cc}\to\mathrm{circ}} = 0.1$ and $\mathrm{intra}_{\mathrm{circ}\to\mathrm{cc}} = 0$ (right plot).

We defined the following parameters for the amplitude and relaxation of the circadian clock and cell cycle: $\lambda = A_\mathrm{o} = \gamma = B_\mathrm{o} = 1$ in all figures. However, in Supplementary Figs. 4d and 6g, to account for heterogeneity and more realistic biological interactions within the ensemble, we simulated the parameters γ and B_o using a normal distribution with different means within the range [0.5, 1.5] and a 0.1 dispersion. For λ and A_o, we used a normal distribution with mean 1 and dispersion 0.1, for $t_\mathrm{f} = 700$ and $N = 200$.

The periods were defined as T_circ for the circadian clock and IMT for the length of the cell cycle. For Fig. 2g and Supplementary Fig. 4a,b, the periods were obtained randomly from a Gaussian distribution with a mean of 22 h (T_circ, circadian clock) and 26 h (IMT, cell cycle) and a standard deviation of $\sqrt{6}$ h (both). For Fig. 2b left, to simulate a network of circadian oscillators, we used Poincaré equations for the circadian clock with mean-field coupling (equations (2) and (4)). The circadian clock periods (T_circ) were obtained randomly from a Gaussian distribution with a mean of 24 h and a dispersion between 0 and 10 h. For Fig. 2b (right) and Fig. 2c, a network of circadian oscillators was simulated using equations (2) and (4) with the T_circ (circadian clock) and IMT (cell cycle) periods obtained randomly from a Gaussian distribution with means of 22 h and 26 h, respectively, and a dispersion of 6 h. For Fig. 2g, we simulated a network of oscillators using equations (2)–(4). The periods were obtained randomly from a Gaussian distribution with various means for the circadian clock (20–28 h) and the cell cycle (28–20 h) and a dispersion of 4 h (both).

For Fig. 2b,g and Supplementary Fig. 4a,b, the initial conditions were randomly distributed between −1 and 1. For Fig. 2b,c, the initial conditions were randomly distributed between −1 and 1 and followed by an initial pulse (first 10 h) of a Gaussian function of 0.01 amplitude, 0 h mean and standard deviation of 2 h.

We used the parameters in Table 1 for the different figures.

Locking and coupling structures. For Fig. 2b, the synchronization index was measured with the following formula:

$$R = \frac{\langle \bar{X}^2 \rangle - \langle \bar{X} \rangle^2}{\frac{1}{N}\sum_{i=1}^{N}\left(\langle X_i^2 \rangle - \langle X_i \rangle^2\right)}.$$

The synchronization index quantifies the extent of coherence among coupled oscillators by contrasting the global variance of averaged values with the mean of individual variances. Here, the numerator represents the variance of the collective behaviour, whereas the denominator accounts for the average variability of the individual components. This metric evaluates the average dynamics over the entire simulation, resulting in a single average value. It focuses exclusively on the x coordinate of the circadian clock to assess the synchronization of the entire ensemble. To create a visual representation resembling a 1:1 Arnold's tongue or entrainment region diagram, we chose symmetric values for the x axis.

For Fig. 2g top, we calculated the phase differences between the circadian clock and the cell cycle over time to give a visual evaluation of the transient phase (Supplementary Fig. 4a). This interval was defined as being at least twice the circadian period (approximately 48 h), during which the oscillators progressed toward their final state from the initial conditions. To ensure accuracy and to avoid including this transient phase, we focused on the second half of the simulations (after 60 h). We then computed the mean phase coherence of the phase differences within the network of oscillators. We defined this measure as the locking index. Finally, the locking index values were visualized as a heat map (Fig. 2g top).

For Fig. 2g right, we computed the individual phase differences between the circadian clock and the cell cycle for each simulated cell unit. After excluding the transient stage, we analysed the individual phase differences beyond 60 h of simulation. A stable internal locking of the circadian clock and cell cycle was defined as having a phase difference dispersion smaller than 0.5. Finally, we calculated the fraction of oscillators that were internally locked within the network and displayed these values as a heat map.

Voronoi diagrams. To characterize and quantify the spatial distribution of cells at different seeding densities, we computed Voronoi diagrams based on the median cell positions over time (Supplementary Fig. 3). We then calculated the area for each cell, grouped the results by condition and presented the data as both a distribution and a bar plot with the mean and standard deviation (Supplementary Fig. 3b,c).

Circadian rhythm properties

Fraction of oscillating cells. A cell was considered to be oscillating if it had at least one oscillation of 24 h with a mean wavelet power of 10 (a.u.). The peaks were found with the function find_peaks and the parameters (height 0, distance 32 and prominence 0.1) from the preprocessed circadian signals.

Population circadian amplitude. The population oscillation represented in Fig. 2b,d,e was obtained by summing the individual detrended and amplitude-normalized circadian oscillations and dividing by N.

Population period. The instantaneous period of the population circadian oscillation was obtained using a continuous wavelet transform with the function compute_spectrum from the pyBOAT package of Python. This function identifies the dominant rhythm with the highest power within the range 16–32 h. We chose this range to capture an 8-h interval around the circadian period to avoid bias. Once the predominant period had been found, the resulting curve was smoothed using the sinc_smooth function from the same package with a cutoff period of 5 h for the simulated periods or 10 h for the experimental data.

Instantaneous amplitudes. Instantaneous amplitudes from Supplementary Fig. 1f,g at the single-cell level were computed using a continuous wavelet transform with the function compute_spectrum from the pyBOAT package of Python. We used the detrended signals obtained from the function sinc_detrend (with a cutoff period of 50 h).

Phase coherence. The phase coherence was computed with the following formula:

$$r = \frac{1}{N}\left|\sum_j e^{i\theta_j}\right| \quad (5)$$

for Fig. 2c,g (top) and Supplementary Fig. 4a,b. We considered the formula for the order parameter from the Kuramoto model. The phase coherence quantifies the phase alignment among oscillators over time. It provides the instantaneous average phase of the ensemble. For Fig. 2j and Supplementary Fig. 3d, it was plotted using the function get_ensemble_dynamics from the same pyBOAT package. This computational function employs the same formula as in equation (5).

Single-cell periods. The instantaneous periods were extracted using a continuous wavelet transform from the preprocessed circadian signals. The instantaneous periods are depicted in Supplementary Fig. 1a,b using the function boxplot from the Python Seaborn package[63].

Circadian and cell cycle locking metrics

Phase differences. The phase differences were calculated as follows:

$$\text{phase diff} = \text{atan2}(\sin(\text{circ} \to \text{cc}), \cos(\text{circ} \to \text{cc})). \quad (6)$$

To compute the phase coherence of the phase differences, we used equation (5) and the phase differences from the above formula. For the mean value of the phase coherence of the phase differences, which is defined as the locking index, we avoided the transient stage and took the average from the second part of the simulation.

Phase-space histograms. The phases θ were normalized between 0 and 1 by dividing by 2π. A two-dimensional histogram was created with the NumPy[64] function histogram2d and plotted with the imshow function from Matplotlib with a bilinear interpolation for simulations or by using the function hist2d from Matplotlib for experimental data.

Correlation coefficients between histograms. We established the phase representation histogram of an untreated high-seeded cell population as a reference. We conducted a comparative analysis of alternative experimental conditions against this baseline by computing the correlation coefficient between flattened two-dimensional histograms with the function corrcoef from NumPy. We flattened a two-dimensional histogram by converting it into a one-dimensional array while preserving the order of the elements with the flatten function in Python.

Normalized phase coherence and detuning. The circadian phase coherence was computed with equation (5) and normalized with the maximum value. The phase differences between the circadian and the cell cycle were computed using equation (6). The phase coherence of these phase differences was computed using equation (5) and normalized with the maximum value. The detuning between the circadian and the cell cycle was computed as the population average from the single-cell period difference between the circadian clock and the cell cycle.

Growth metrics

Growth curves. The growth curves were measured from the cell confluence using the software Incucyte and were smoothed using the function savgol_filter (window_length = 9 and polyorder = 2) from the Python package SciPy signal (ref. 65; Fig. 3b,e and Supplementary Fig. 5g,h).

Fitting growth and division curves. A sigmoidal growth function

$$f(t) = \frac{K}{1 + ((K - N_0)/N_0)\, e^{-rt}}$$

was used to fit the growth and cumulative division curves, where K denotes the growth saturation, N_0 is the initial growth and r is the growth rate. The fitting was achieved using the function curve_fit from the SciPy signal library. From the growth rates, we obtained the doubling times with the following formula $T_d = \ln 2/r$, and the error was computed using the error propagation formula. We used a linear fit for the first 24 h of growth: $f(t) = rt + a$.

Proliferation plots. Division matrices were constructed to encode division events (assigned a value of 1) and instances of non-proliferation (assigned a value of 0). Cells were grouped based on the number of divisions, and within each division group, they were sorted according to the time at which the initial mitosis occurred (Fig. 4a).

Intermitotic distributions. The IMTs were obtained from the individual cell cycles using a continuous wavelet transform. We chose the cells that were tracked from the beginning of the experiment for each condition and built a histogram using the Python function histplot from the Seaborn package.

Cumulative distribution of division events. A random equal sample of cells was bootstrapped from each condition. We summed all the condensed division events of the cells over time to avoid potential effects

due to sampling size. We computed the cumulative sum of these division events with the Python function cumsum. To obtain the average cumulative distributions, this process was iterated 100 times. Finally, all the conditions were normalized to the maximum of the cumulative distribution of the untreated condition.

Detrended cumulative distribution of division events and periods. The cumulative distribution of division events was detrended using the function sinc_detrend (with a cutoff period of 40 h) and smoothed with the function sinc_smooth (with a cutoff period of 10 h) from pyBOAT. The period was extracted with a continuous wavelet transform using the function compute_spectrum (from pyBOAT) in the range between 16 and 32 h and presented in a box plot.

Relative growth. The relative growth was obtained by dividing the untreated confluence by the treated confluence and smoothed with the function savgol_filter (window_length = 9 and polyorder = 2) from the SciPy signal package in Python.

Simulations of IMT and circadian distributions. We simulated various scenarios to examine how the distributions of the lengths of the cell cycle changed for different values of the extracellular circadian coupling (extra = 0 for Supplementary Fig. 7a,c and extra = 0.7 for Supplementary Fig. 7b,d). For these simulations, we used Gaussian distributions for the free-running period of the circadian oscillators, with a mean of 24 h and a dispersion of 6 h, and IMT distributions with a mean of 16 h for Supplementary Fig. 6a,b and 32 h for Supplementary Fig. 6c,d and a dispersion of 6 h. For the simulations, we considered $N = 200$ oscillators, $t_f = 400$ and $dt = 0.1$.

Mathematical model of the circadian cell cycle modulation

We wanted to keep the model of the cell cycle simple while still being able to respond diversely depending on how the coupling between the cell cycle and a circadian rhythm was configured. To do so, the cell cycle was broken down into two phases (G1 and G2), and two instantaneous transitions between phases (S and M). We modelled this system with a set of coupled differential equations:

$$dG_1 = K_{G1}(1 - S) - C_1 \frac{G_1}{G_1 + C_2},$$

$$dS = K_S \max(G_1 - C_3, 0)(1 - S),$$

$$dG_2 = K_{G2} S,$$

$$dM = K_M \frac{1}{1 + \exp(-C_4(G_2 - C_5))}.$$

Using a Gillespie approach, we simulated the cell cycle as a stochastic system. The randomness of the simulation was changed by altering the 'volume' of the system. A smaller volume will lead to a more stochastic result. We chose the K and C parameters for the system to give a self-sustained period of roughly 22 h (see table below for values). The circadian rhythm was generated using the same approach as equations (2) and (3). To ensure we had a positive-valued circadian signal, we transformed the sine-like signal (OSC) as

$$\text{circadian}(t) = \left(\left(\frac{1}{2} + \frac{\text{OSC}(t)}{2}\right)^2\right). \quad (7)$$

To couple the cell cycle model and the circadian, either we coupled to the speed of cell cycle progression, by coupling to either K_{G1} or K_{G2}, or we introduced a time-dependent gating mechanism by coupling to the gating parameters K_S or K_M. Both introduce a delay to the cell cycle progression, but in two different ways. The coupling strength was modulated using the coupling parameter α such that

$$\widetilde{K} = K(\alpha + (1 - \alpha)\,\text{circadiant}(t)),$$

where $\widetilde{K}$ is the circadian-modulated parameter K

Name	K_{G1}	K_S	K_{G2}	K_M	C_1	C_2	C_3	C_4	C_5	Volume
Value	50	0.5	0.3	0.4	20	100	GMAX	1	10	2

To initially match the circadian rhythm and the length of the cell cycle, the parameter GMAX for each cell cycle was altered using

$$\text{GMAX} = 3.8T_{\text{Circadian}} + \text{ExpGauss}(0, 0, 0.005)$$

with ExpGauss being a random exponential modified Gaussian number drawn from the following equation, where μ represents the mean, σ is the spread and λ is the decay.

$$f(x; \mu = 0, \sigma = 0, \lambda = 0.005) = \frac{2}{\lambda} \exp\left(2\mu + \lambda\sigma^2 - 2x\right) \text{erfc}\left(\frac{\mu + \lambda\sigma - x}{\sqrt{2\sigma}}\right). \quad (8)$$

Fit

We simulated cell cycles with 800 individually simulated cells. Each cell underwent cell division when passing the M transition in the cell cycle. The distribution (Fig. 4f) of intermitotic periods was subsequently fitted to an exponentially modified Gaussian distribution (equation (8)) using a binned χ^2 method. From these parameters, we calculated the mean of a distribution as

$$\mu_{\text{True}} = \mu + \frac{1}{\lambda}.$$

Likewise, we computed the error of the mean using standard error propagation with the parameter correlation found while fitting.

Cumulative growth

We subdivided the simulation into small time steps and measured how many cells underwent mitosis during each time step. Computing the cumulative number of divisions gave a linear growth number indicating the number of divisions for all cells at a given time. This signal was then detrended by subtracting a linear trend of the signal.

Reporting summary

Further information on research design is available in the Nature Portfolio Reporting Summary linked to this article.

Data availability

All the data generated and used for this investigation are available via Figshare at https://doi.org/10.6084/m9.figshare.28375358.v1 (ref. 66).

Code availability

The code used in this study can be found at https://github.com/Granada-Lab/Circadian-clock-cell-cycle and https://github.com/Granada-Lab/Automatic-single-cell-tracking-of-fading-objects. We used Python v.3.8.8. and the following packages: Seaborn (v.0.11.2), Matplotlib (v.3.6.3), NumPy (v.1.23.3), pandas (v.1.4.4), SciPy (v.1.9.1), Skimage (v.0.20.0) and pyBOAT (v.0.9.1).

References

60. Rogatsky, I., Hittelman, A. B., Pearce, D. & Garabedian, M. J. Distinct glucocorticoid receptor transcriptional regulatory surfaces mediate the cytotoxic and cytostatic effects of glucocorticoids. *Mol. Cell. Biol.* **19**, 5036 (1999).

61. Haubold, C. et al. in *Focus on Bio-Image Informatics* (eds De Vos, W. H. et al.) 199–229 (Springer, 2016).
62. Mönke, G., Sorgenfrei, F. A., Schmal, C. & Granada, A. E. Optimal time frequency analysis for biological data – pyBOAT. Preprint at *bioRxiv* https://doi.org/10.1101/2020.04.29.067744 (2020).
63. Waskom, M. Seaborn: statistical data visualization. *J. Open Source Softw.* **6**, 3021 (2021).
64. Harris, C. R. et al. Array programming with NumPy. *Nature* **585**, 357–362 (2020).
65. Virtanen, P. et al. SciPy 1.0: fundamental algorithms for scientific computing in Python. *Nat. Methods* **17**, 261–272 (2020).
66. Gutu, N. RawData_Gutu_et_al_Circadian_Coupling_Orchestrates_Cell_growth. *Figshare* https://doi.org/10.6084/m9.figshare.28375358.v1 (2025).

Acknowledgements

We would like to extend our gratitude to H.-Y. Liou for his invaluable assistance in the establishment of the automatic tracking pipeline with ilastik. We thank the AMBIO imaging facility of the Charité Berlin for support in the acquisition of real-time fluorescence data. This work was financially supported by the German Federal Ministry for Education and Research through the e:Med Juniorverbund DeepLTNBC TP 3 - 01ZX1917C programme. M.S.N. and M.H.J. acknowledge support from the Independent Research Fund Denmark (Grant No. 9040-00116B) and the Novo Nordisk Foundation (Grant No. NNF20OC0064978). M.S.H. acknowledges support from the Lundbeck Foundation. C.E. is thankful for the support of the Berlin School of Integrative Oncology.

Author contributions

N.G. and A.E.G. were responsible for conceptualization and investigation. N.G., M.S.N. and A.E.G. were responsible for developing the methodology. The experiments were run by N.G., M.K., C.E., M.M. and A.F. The results were visualized by N.G. and A.E.G. A.E.G., M.H.J. and M.S.H. acquired funding. The project was administered and supervised by A.E.G. N.G. and M.S.N. wrote the original draft of the manuscript. N.G., M.S.N., C.E. and A.E.G. reviewed and edited the manuscript. Intellectual support was provided by U.K., A.K., M.H.J., M.S.H. and H.H.

Competing interests

The authors declare no competing interests.

Additional information

Supplementary information The online version contains supplementary material available at https://doi.org/10.1038/s41567-025-02838-4.

Correspondence and requests for materials should be addressed to Adrián E. Granada.

nature portfolio

Corresponding author(s): Adrian E. Granada

Last updated by author(s): Feb 12, 2025

Reporting Summary

Nature Portfolio wishes to improve the reproducibility of the work that we publish. This form provides structure for consistency and transparency in reporting. For further information on Nature Portfolio policies, see our Editorial Policies and the Editorial Policy Checklist.

Statistics

For all statistical analyses, confirm that the following items are present in the figure legend, table legend, main text, or Methods section.

n/a	Confirmed
☐	☒ The exact sample size (*n*) for each experimental group/condition, given as a discrete number and unit of measurement
☐	☒ A statement on whether measurements were taken from distinct samples or whether the same sample was measured repeatedly
☐	☒ The statistical test(s) used AND whether they are one- or two-sided *Only common tests should be described solely by name; describe more complex techniques in the Methods section.*
☒	☐ A description of all covariates tested
☒	☐ A description of any assumptions or corrections, such as tests of normality and adjustment for multiple comparisons
☐	☒ A full description of the statistical parameters including central tendency (e.g. means) or other basic estimates (e.g. regression coefficient) AND variation (e.g. standard deviation) or associated estimates of uncertainty (e.g. confidence intervals)
☐	☒ For null hypothesis testing, the test statistic (e.g. *F*, *t*, *r*) with confidence intervals, effect sizes, degrees of freedom and *P* value noted *Give P values as exact values whenever suitable.*
☒	☐ For Bayesian analysis, information on the choice of priors and Markov chain Monte Carlo settings
☒	☐ For hierarchical and complex designs, identification of the appropriate level for tests and full reporting of outcomes
☒	☐ Estimates of effect sizes (e.g. Cohen's *d*, Pearson's *r*), indicating how they were calculated

Our web collection on statistics for biologists contains articles on many of the points above.

Software and code

Policy information about availability of computer code

Data collection	Incucyte analysis software (Sartorius, v2022A), for acquisition and image analysis of population live-cell imaging data. Single-cell live imaging was achieved utilizing NIS-Elements visualization software (Nikon). The experimental raw data and data tables generated in this study have been deposited in the Figshare database under the identifier: https://doi.org/10.6084/m9.figshare.28375358.v1
Data analysis	The implemented code used for this study can be found here: https://github.com/Granada-Lab/Circadian-clock-cell-cycle and https://github.com/Granada-Lab/Automatic-single-cell-tracking-of-fading-objects. For this study we used Python v.3.8.8. and the following packages: Seaborn (v0.11.2), Matplotlib (v3.6.3), NumPy (v1.23.3), pandas (v1.4.4), SciPy (v1.9.1), Skimage (v0.20.0), and pyBOAT (v0.9.1).

For manuscripts utilizing custom algorithms or software that are central to the research but not yet described in published literature, software must be made available to editors and reviewers. We strongly encourage code deposition in a community repository (e.g. GitHub). See the Nature Portfolio guidelines for submitting code & software for further information.

Data

Policy information about availability of data

All manuscripts must include a data availability statement. This statement should provide the following information, where applicable:

- Accession codes, unique identifiers, or web links for publicly available datasets
- A description of any restrictions on data availability
- For clinical datasets or third party data, please ensure that the statement adheres to our policy

All the data generated and used for this investigation is available at the following link:
https://doi.org/10.6084/m9.figshare.28375358.v1

Research involving human participants, their data, or biological material

Policy information about studies with human participants or human data. See also policy information about sex, gender (identity/presentation), and sexual orientation and race, ethnicity and racism.

Reporting on sex and gender	N/A
Reporting on race, ethnicity, or other socially relevant groupings	N/A
Population characteristics	N/A
Recruitment	N/A
Ethics oversight	N/A

Note that full information on the approval of the study protocol must also be provided in the manuscript.

Field-specific reporting

Please select the one below that is the best fit for your research. If you are not sure, read the appropriate sections before making your selection.

☒ Life sciences ☐ Behavioural & social sciences ☐ Ecological, evolutionary & environmental sciences

For a reference copy of the document with all sections, see nature.com/documents/nr-reporting-summary-flat.pdf

Life sciences study design

All studies must disclose on these points even when the disclosure is negative.

Sample size	Sample size was not pre-determined, but we obtained itbased on automated tracking, which allowed us to extract circadian and cell cycle signals at the single-cell level. According to the standards in the field, two independent live-imaging experiments were conducted with two to three technical replicates.
Data exclusions	Data was retained for analysis except when identified as outliers through statistical testing.
Replication	Live-imaging experiments were carried out a single time because of the comprehensive data generated. The evaluation of each condition was based on a detailed analysis of the captured individual images.
Randomization	Randomization was applied during bootstrapping to ensure that the resampled datasets were representative. For other experiments, allocation into experimental groups was not randomized as the study did not involve large cohorts for treatment and control groups. We did not consider potential covariates rellevant to our experiments.
Blinding	Investigators were not blinded to group allocation during either data collection or analysis. Given the nature of the data and the analytical methods used, blinding was not deemed relevant to the integrity or objectivity of the study results.

Reporting for specific materials, systems and methods

We require information from authors about some types of materials, experimental systems and methods used in many studies. Here, indicate whether each material, system or method listed is relevant to your study. If you are not sure if a list item applies to your research, read the appropriate section before selecting a response.

Materials & experimental systems

n/a	Involved in the study
☒	☐ Antibodies
☐	☒ Eukaryotic cell lines
☒	☐ Palaeontology and archaeology
☒	☐ Animals and other organisms
☒	☐ Clinical data
☒	☐ Dual use research of concern
☒	☐ Plants

Methods

n/a	Involved in the study
☒	☐ ChIP-seq
☒	☐ Flow cytometry
☒	☐ MRI-based neuroimaging

Eukaryotic cell lines

Policy information about cell lines and Sex and Gender in Research

Cell line source(s)	U2OS (human, ATCC # HTB-96) and (human, T-Rex Life technologies R712-07). U-2 OS circadian reporter cell line were gifted by M. Brunner Lab, Heidelberg University, Germany. U-2 OS wild-type and Cry1/Cry2-dKO were provided by the Kramer lab, Charité, Berlin, Germany. HaCaT keratinocytes were gifted from Dr Fusenig Lab, Deutsches Krebsforschungsinstitut, Heidelberg, Germany. NIH3T3 were purchased from the American Type Culture Collection (atcc.org/products/crl-1658). HEK293T cells were gifted by the Lahav lab, Harvard Medical School, Boston, USA.
Authentication	The cells were authenticated using SNP-typing technology, Multiplexion GmbH.
Mycoplasma contamination	Cell lines were tested for mycoplasma contamination and showed no infection, nor any signs of health decline.
Commonly misidentified lines (See ICLAC register)	No commonly misidentified cell line was used in this study.

Plants

Seed stocks	n/a
Novel plant genotypes	n/a
Authentication	n/a